Electronic structure and low-temperature study of the $Ce_{1-x}La_xRh_4Sn_{13}$

A. Ślebarski, P. Witas, J. Goraus, L. Kalinowski, and M. Fijałkowski
Institute of Physics, University of Silesia, 40-007 Katowice, Poland
(Received 8 May 2014; revised manuscript received 29 July 2014; published 13 August 2014)

Recently, it was reported that the skutterudite-related $Ce_3Rh_4Sn_{13}$ heavy fermion compound has a large electronic specific heat coefficient $C(T)/T$ and short-range magnetic correlations, both suggest a possible quantum critical point (QCP). We present the low-temperature specific heat, resistivity, and susceptibility of $Ce_{1-x}La_xRh_4Sn_{13}$, which do not confirm the presence of QCP. X-ray photoelectron spectroscopy revealed a stable configuration of Ce atoms consistent with magnetic susceptibility data. Magnetic susceptibility shows that the sixfold-degenerate multiplet of Ce^{3+} ion splits into three doublets due to the lower local symmetry of $CeSn_{12}$ cage in the cubic $Ce_{1-x}La_xRh_4Sn_{13}$ compounds. The resistivity, specific heat, and susceptibility data are consistent with our band-structure calculations. The chemical bondings in the unit cell of $Ce_{1-x}La_xRh_4Sn_{13}$, analyzed based on the difference charge density maps from band-structure calculations within the virtual crystal approximation explain the deformation of the cages and the crystal electric field properties of the system.

DOI: 10.1103/PhysRevB.90.075123 PACS number(s): 71.27.+a, 72.15.Qm

I. INTRODUCTION

Comprehensive studies of both electronic band-structure and low-temperature physical properties of Ce-based heavy fermions are of fundamental importance in the last few decades for understanding of their thermodynamic and transport characteristics. The important cause of various and novel ground states is the transition between the itinerant and localized character of heavy electrons, the nature of this itinerant-localized f-electron evolution seems to be an outstanding problem in the strongly correlated electron systems. As a good example, a metal-insulator transition of the Mott-Hubbard type represents such a behavior, since it exemplifies a transition from well defined localized atomic states to delocalized Bloch- or Fermi-liquid-type of states [1] under a relatively small change in temperature, alloy composition, or pressure. Localized f electrons have a tendency to form magnetically ordered states with an exchange interaction of RKKY type, while the itinerant character arises from the Kondo effect with a spin singlet. Very interesting is the case near the quantum critical point (QCP) where the itinerant and localized character compensates, and near-equivalent Kondo and magnetic ordering energy scales provide an opportunity to test our understanding of the interplay between these competing interactions. Recently, it was found that the skutterudite-related $Ce_3M_4Sn_{13}$ heavy fermions (M = Co and Rh) show a behavior characteristic of the Ce-based materials with comparable Kondo and magnetic energy scales. Specific-heat, magnetic susceptibility, and electric transport data indicated for both compounds low-temperature antiferromagnetic correlations (without long-range magnetic order) and Kondo effect with a Kondo temperature of about 1.5 K [2,3]. Moreover, a large electronic specific-heat coefficient $C(T)/T$ has suggested that both $Ce_3Co_4Sn_{13}$ and $Ce_3Rh_4Sn_{13}$ can be near a magnetic QCP [4]. For that reason, these materials are interesting for detailed investigations of the electronic structure and its consequences on electric transport and low-temperature thermodynamic properties. In order to study the expected quantum criticality of $Ce_3Rh_4Sn_{13}$, we investigated the low-temperature specific heat and resistivity of $Ce_{3-x}La_xRh_4Sn_{13}$ and showed that partial substitution of Ce by larger La does not induce any long-range magnetic order in the system, although the unit-cell volume increases linearly with increasing x, and the low-temperature behaviors are not characteristic of the QCP. We, however, found that with increasing of La content the system evolves from a magnetically correlated Kondo lattice state to a single-ion Kondo impurity state. To understand the specific heat data and the complexity of the $Ce_{3-x}La_xRh_4Sn_{13}$ system, we base our analysis on the Anderson [5] and Kondo [6] theoretical models. To gain deeper insight into the character of the Ce $4f$ states, we present x-ray photoemission spectroscopy (XPS) spectra and analyze the hybridization strength between the Ce $4f$ shell and the conduction states. The valence-band (VB) XPS spectra we compare with the *ab initio* band-structure calculations. The chemical bondings between different atoms in the unit cell of $Ce_{3-x}La_xRh_4Sn_{13}$ are analyzed based on the difference charge density maps obtained from band-structure calculations within the virtual crystal approximation (VCA).

II. EXPERIMENTAL DETAILS

The $Ce_3Rh_4Sn_{13}$ and $La_3Rh_4Sn_{13}$ samples were first prepared by arc melting weighed amounts of each component. The dilute $Ce_{3-x}La_xRh_4Sn_{13}$ alloys were then prepared by diluting nominal compositions of the parent compounds. To ensure homogeneity, each sample was turned over and remelted several times and then annealed at 870 °C for 2 weeks. All samples were carefully examined by x-ray diffraction analysis and found to be single phase with cubic structure (space group $Pm\bar{3}n$) [7]. As shown in Fig. 1, the unit cell contains two formulas of $Ce_3Rh_4Sn_{13}$ with Sn1, Ce, Rh, and Sn2 atoms occupying the $2a$, $6d$, $8e$, and $24k$ sites, respectively (only the Sn2 atoms are not located at the most stable positions). XRD data were refined using FULLPROF program [8] with pseudo-Voight line shape. The conventional Bragg factors R of the structure refinements were all smaller than 0.05. A refinement of the Bragg peaks in the scattering angle range $10^\circ \leqslant 2\theta \leqslant 100^\circ$ yield the lattice parameter a for each component x with an accuracy $\sim 3 \times 10^{-4}$ Å. The x-ray diffraction pattern obtained for $Ce_3Rh_4Sn_{13}$ was presented recently [9], the room-temperature XRD on the $Ce_{3-x}La_xRh_4Sn_{13}$ are similar. Figure 2 displays a versus x

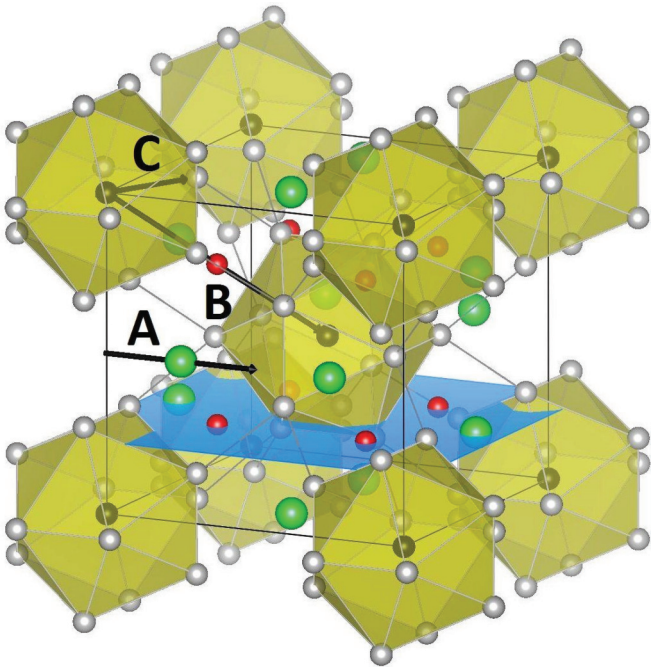

FIG. 1. (Color online) The unit-cell structure of $Ce_3Rh_4Sn_{13}$. Ce atoms are shown as larger green balls, Rh atoms as red balls, Sn2 are gray, and Sn1 are dark green balls.

obtained from the room-temperature data collection, with an error bar determined by the experimental accuracy of $\Delta\theta = 0.005^\circ$ for each XRD pattern. The lattice parameters of $Ce_{3-x}La_xCo_4Sn_{13}$ follow Vegard law, which suggests that the samples x are good quality and stoichiometric.

Electrical resistivity ρ was investigated by a conventional four-point ac technique using a Quantum Design Physical Properties Measurement System (PPMS). Electrical contacts were made with 50-μm-gold wire attached to the samples by spot welding.

Specific heat C was measured in the temperature range 0.4–300 K and in external magnetic fields up to 9 T using a Quantum Design PPMS platform. Specific-heat $C(T)$ measurements were carried out on platelike specimens with masses of about 10–15 mg utilizing a thermal-relaxation method. The dc magnetization M and magnetic susceptibility χ results were obtained using a commercial superconducting quantum interference device magnetometer from 1.8 to 300 K in magnetic fields up to 7 T.

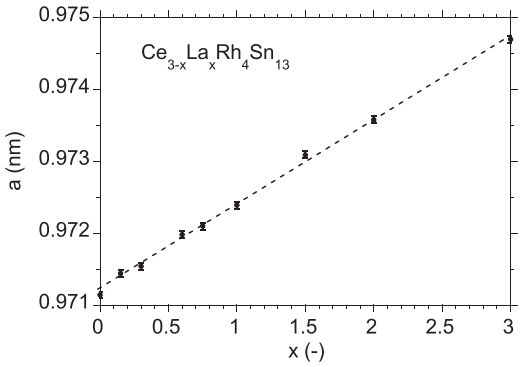

FIG. 2. The lattice parameters of $Ce_{3-x}La_xRh_4Sn_{13}$ measured at 300 K vs concentration of La (x).

The XPS spectra were obtained with monochromatized Al K_α radiation at room temperature using a PHI 5700 ESCA spectrometer. The polycrystalline sample was broken under high vacuum better than 6×10^{-10} Torr immediately before taking a spectrum.

The band-structure calculations were accomplished using the fully relativistic full potential local orbital (FPLO) method (FPLO9-00-34 computer code [10]) within the local spin density approximation (LSDA). The exchange correlation potential V_{xc} was used in the form proposed by Perdew and Wang [11]. The number of k points in the irreducible wedge of Brillouin zone was 20 for each component of the series, due to a large volume of the unit cell this number was found sufficient to obtain well converged results. The spin-orbit interactions considered within fully relativistic calculations reduce the symmetry of the magnetic unit cell depending on the chosen magnetization axis. In our calculations we used (0,0,1) as the chosen direction of the magnetization axis. The charge density was evaluated on a $52 \times 52 \times 52$ point grid within the unit cell.

III. RESULTS AND DISCUSSION

A. Electronic structure: experiment and calculations

Recently [12], we presented the electronic structure of $Ce_3Rh_4Sn_{13}$ and $La_3Rh_4Sn_{13}$, here we are more concentrated on the band structure of the $Ce_{3-x}La_xRh_4Sn_{13}$ alloys in order to explain the influence of alloying on the covalent bonding between the atoms in the unit cell. Valence band (VB) XPS spectra are shown in Fig. 3(a). The spectra are very similar for all components of the series, which suggests that the Ce $4f$ states should give only a small contribution to the measured VB XPS spectra. Figure 3(b) shows the calculated total spin-resolved densities of states (DOS) obtained for $Ce_{3-x}La_xRh_4Sn_{13}$ within LSDA approximation. The results confirm small f-electron contribution to the measured spectra as compared to the other VB states, therefore such a slight signal of f-electron origin can not be distinctly detected. Consequently, the VB XPS spectra are not decisive with respect to the localization of the $4f$ states in the valence bands of $Ce_{3-x}La_xRh_4Sn_{13}$. The most intense peak in VB XPS originates mainly from Rh $4d$ states, there are also some contributions from the Sn $5p$ electrons, and from the effect of hybridization between Rh d electron and Sn p-electron states. The second broad and weak maximum centered at $\sim$7 eV is related to photoemission from Sn $5s$ states.

The Ce-$3d$ core level photoemission is more useful to demonstrate the nature of localized/delocalized character of the Ce $4f$ states in Ce-based intermetallics owning to strong Coulomb interaction between the photoemission core hole and the electrons located near the Fermi level. This coupling results in a complex structure of the Ce core level $3d$ XPS spectra, as a result we observe the main $3d^9_{5/2}4f^1$ and $3d^9_{3/2}4f^1$ spin-orbit components of the final states associated with the stable configuration of the Ce-f shell (Ce^{3+}) and the contributions $3d^94f^0$ and $3d^94f^2$ due to the on-site hybridization between the f-electron states and the conduction band. The presence of the contribution $3d^94f^0$ indicates an intermediate character of

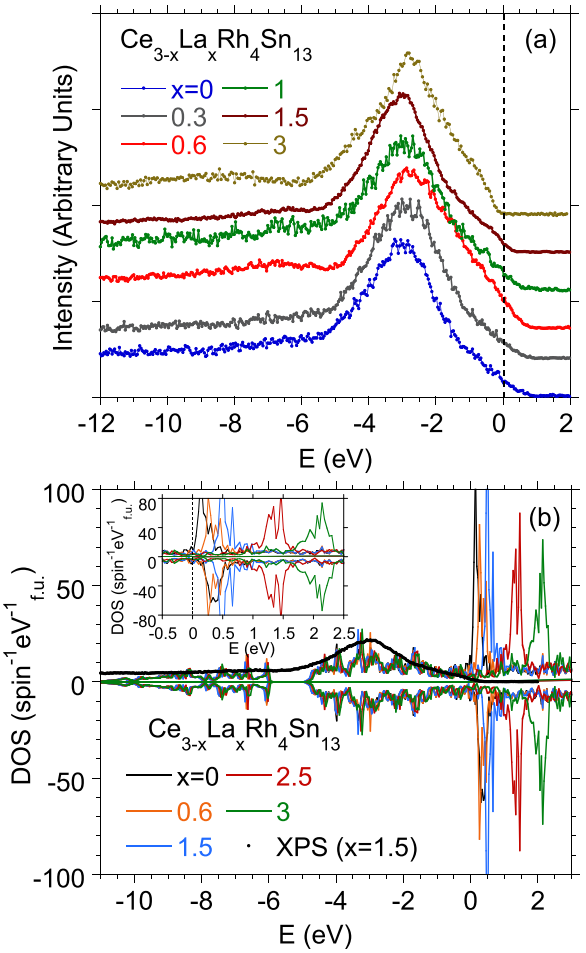

FIG. 3. (Color online) $Ce_{3-x}La_xRh_4Sn_{13}$ valence-band XPS spectra (a), which show very similar structure. The VB XPS spectrum of $Ce_{1.5}La_{1.5}Rh_4Sn_{13}$ is compared with the calculated total and spin-resolved density of states within LSDA approximation. The TDOSs are also shown for selected compounds of the series. We note that the energetic distribution of the electronic states is almost not x-dependent, while the location of empty f-electron states evidently depends on alloying.

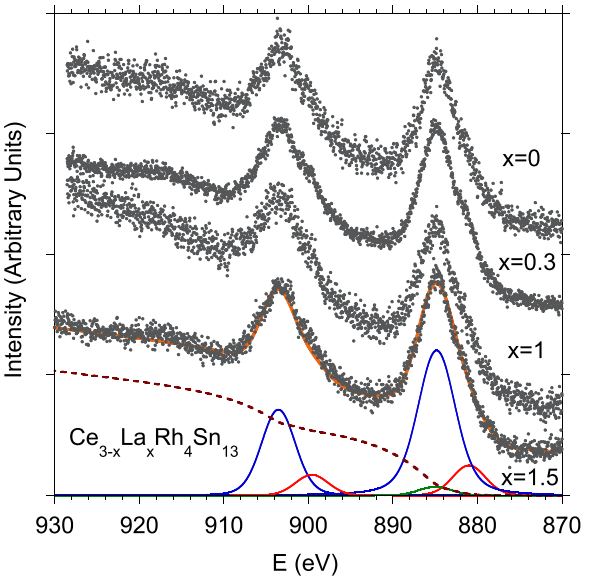

FIG. 4. (Color online) $Ce_{3-x}La_xRh_4Sn_{13}$; the Ce $3d$ XPS spectra measured at the room temperature. The XPS spectrum of $Ce_{1.5}La_{1.5}Rh_4Sn_{13}$ is deconvoluted, based on the Gunnarsson-Schönhammer theoretical model and displays SO components $3d^9 4f^1$ (blue line), $3d^9 4f^2$ (red line). The Sn $3s$ peak at 885 eV provides ∼15% of the total peak intensity due to $3d^9_{5/2} 4f^1$ final states (green line). The solid yellow line shows the fit after deconvolution to the XPS data.

the Ce ions, while $3d^9 4f^2$ reflects the hybridization strength, $\Delta = \pi V^2 N(\epsilon_F)$. Figure 4 displays the Ce $3d$ XPS spectra for selected $Ce_{3-x}La_xRh_4Sn_{13}$ compounds.

The quantitative analysis of the $3d$ XPS spectra was performed based on the Gunnarsson and Schönhammer (GS) theory, for details see Refs. [13–15]. The analysis of the intensity ratios of the components obtained from deconvolution allowed for the determination of valence (the occupation number of the $4f$ shell, $n_f \cong 1$, suggests a stable configuration Ce^{3+} of the $4f$ shell in the series of $Ce_{3-x}La_xRh_4Sn_{13}$ compounds with $x < 3$) and hybridization energies Δ of about 70 ± 20 meV. The small energy Δ points to the well-localized character of the Ce $4f$ states in the system.

Recently [12], the difference charge density analysis displayed in $Ce_3Rh_4Sn_{13}$ charge accumulations between Rh and Sn2 atoms, which implies a strong covalent bonding interaction. The second type of charge accumulations was calculated between the Sn2 atoms with possible contribution from the surrounding Ce atoms and one Sn1 atom. We also suggested [9] a connection between this charge accumulation in the bonding of nearest-neighboring Sn2 and Rh atoms, leading to a local distortion of the Sn2 cages, which then modifies the electronic structure and divers physical properties of $Ce_3Rh_4Sn_{13}$ and similar compounds. In this work, we investigate the charge accumulation around Ce, Rh, and Sn atoms when the Ce atomic positions are systematically substituted by La. We have calculated the 3D charge density for different components x of the $Ce_{3-x}La_xRh_4Sn_{13}$ series using virtual crystal approximation and FPLO method. Calculations were performed for an effective rare-earth (RE) atom, which had atomic number $Z = 57 + \frac{3-x}{3}$. The following figures represent a linear interpolation of charge density across various directions within the unit cell, based on a $52 \times 52 \times 52$ grid.

Figures 5–8 show the difference in charge density $\Delta\rho_e$, which represents the difference between the crystalline electron density of an $Ce_{3-x}La_xRh_4Sn_{13}$ alloy and the 3D electron density of $La_3Rh_4Sn_{13}$ to illustrate the reorganizing of charge distribution accompanying the bond formation in the system of $Ce_{3-x}La_xRh_4Sn_{13}$ compounds. Figure 5 shows the result in the case of $Ce_{3-x}La_xRh_4Sn_{13}$ along the bonding line A indicated in Fig. 1. As can be expected, the charge density located on Ce atom is proportional to $(3 - x)$, which means that La doping decreases the charge density located on the $6d$ sites. More interesting is the difference charge density fluctuation between Ce atoms, generated by the nearest Sn2 atoms. The amplitude of the charge fluctuation is small, we therefore plot $\Delta\rho_e^{1/4}$ to extend the effect. Figure 6 displays the variation in $\Delta\rho_e$ charge density along the bonding line C between Sn1 and Sn2 atoms. The significant charge accumulation is inside the cage $Sn1(Sn2)_{12}$ between Sn1 and Sn2 atoms, which implies weak

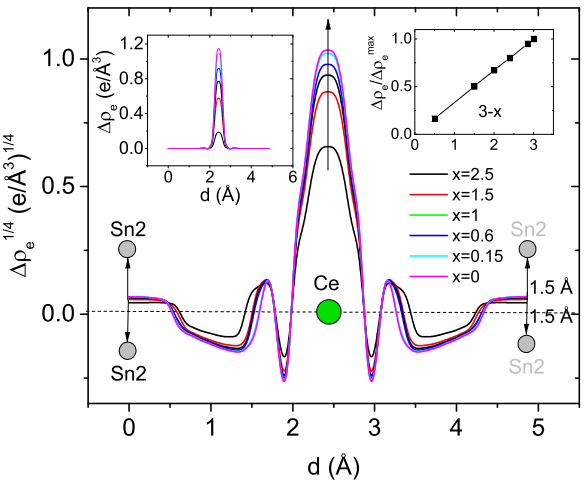

FIG. 5. (Color online) $Ce_{3-x}La_xRh_4Sn_{13}$ charge density $\Delta\rho_e^{1/4}$ near Ce plotted along line *A* (line *A* is drown in Fig. 1). The left and right insets displays the charge accumulation $\Delta\rho_e$ and $\Delta\rho_e/\Delta\rho_e^{\max}$ on the rare-earth atom position 6*d*, respectively, vs La doping, where $\Delta\rho_e^{\max}$ represents the maximum value of difference charge density obtained for $Ce_3Rh_4Sn_{13}$.

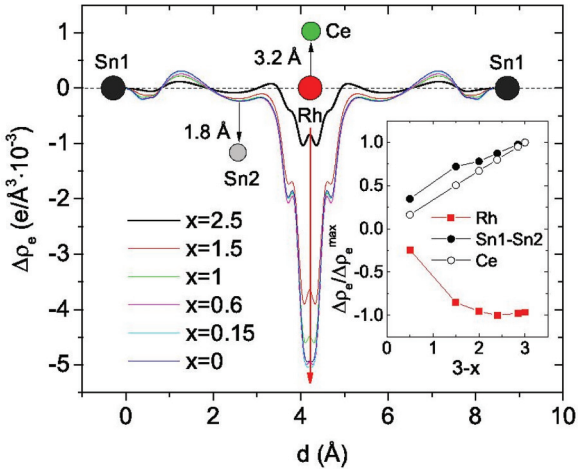

FIG. 7. (Color online) Charge density $\Delta\rho_e$ plotted along line *B* (line *B* is drown in Fig. 1) representing the nearest-neighbor Sn1-Rh-Sn1 bonding. The inset displays the charge accumulation $\Delta\rho_e/\Delta\rho_e^{\max}$ vs La-doping, located on Ce, Rh atoms and in the middle of Sn1-Sn1 distance.

covalent bonding interaction. Figure 7 shows the variation in $\Delta\rho_e$ charge density along the bonding line *B* between Sn1-Rh-Sn1 atoms. For all components of $Ce_{3-x}La_xRh_4Sn_{13}$ with $x > 0$, the difference charge density on Rh is negative and strongly x-dependent, the maximum negative value of $\Delta\rho_e$ is obtained for $Ce_3Rh_4Sn_{13}$. Simultaneously, a high charge density accumulation is observed between Rh and Sn2 atoms (c.f. Figs. 6 and 8), which supports the shift of the charge from the Rh atom to inside the Sn2 cage. Figure 8 shows the map of $\Delta\rho_e$ in the plane $(00\frac{1}{4})$ displayed in Fig. 1. It is clearly visible as a high charge density between Rh and Sn2 atoms, which implies a strong covalent bonding interaction. The bonding features among Rh and Sn2 atoms as well as between Sn1 and Sn2 could cause deformation of $Sn1(Sn2)_{12}$ and $Ce(Sn2)_{12}$ cages, this is indeed observed for $Ce_3Rh_4Sn_{13}$ and similar compounds [9]. A subtle structural transition from a cubic phase to the superlattice variant at about 160 K was observed with accompanying distinct anomalies in the electrical resistivity [3], magnetic susceptibility, and specific heat [9,16], and quantum criticality [17]. In this paper, we are focused on the low-temperature properties of $Ce_{3-x}La_xRh_4Sn_{13}$.

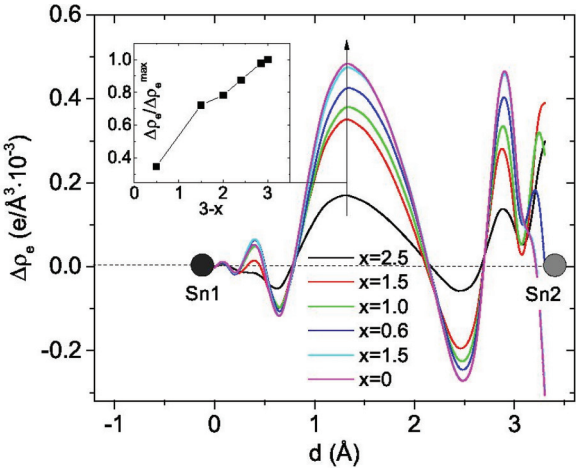

FIG. 6. (Color online) $Ce_{3-x}La_xRh_4Sn_{13}$ charge density $\Delta\rho_e$ plotted along line *C* (line *C* is drown in Fig. 1) between Sn1 and Sn2 atoms. The inset displays the charge accumulation $\Delta\rho_e$ and $\Delta\rho_e/\Delta\rho_e^{\max}$ located between Sn1 and Sn2 vs La-doping, where $\Delta\rho_e^{\max}$ represents the maximum value of difference charge density obtained for $Ce_3Rh_4Sn_{13}$.

B. Magnetic properties of $Ce_{3-x}La_xRh_4Sn_{13}$

The core-level Ce 3*d* XPS spectra give evidence for the stable Ce^{3+} ion configuration in the system of $Ce_{3-x}La_xRh_4Sn_{13}$ alloys, also a relatively small on-site hybridization energy Δ eliminates the valence fluctuation effect of Ce. Our complex research indicates a single-ion Kondo behavior and shows that

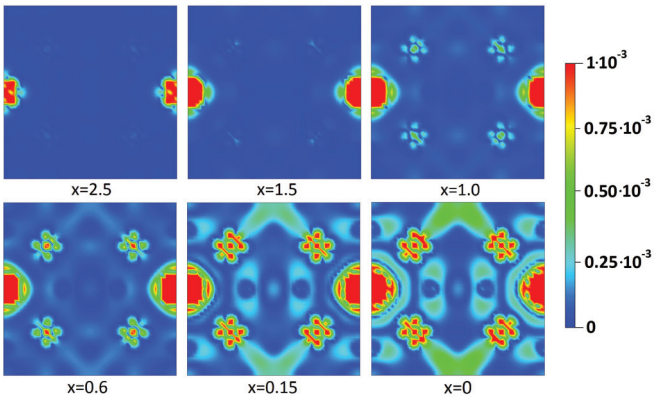

FIG. 8. (Color online) The difference charge densities $\Delta\rho_e$ (electron/Å^3) for the plane $(00\frac{1}{4})$ of $Ce_{3-x}La_xRh_4Sn_{13}$ provided with a legend. The charge density maps reveal that the strongest charge accumulations are located between Rh and Sn2 atoms.

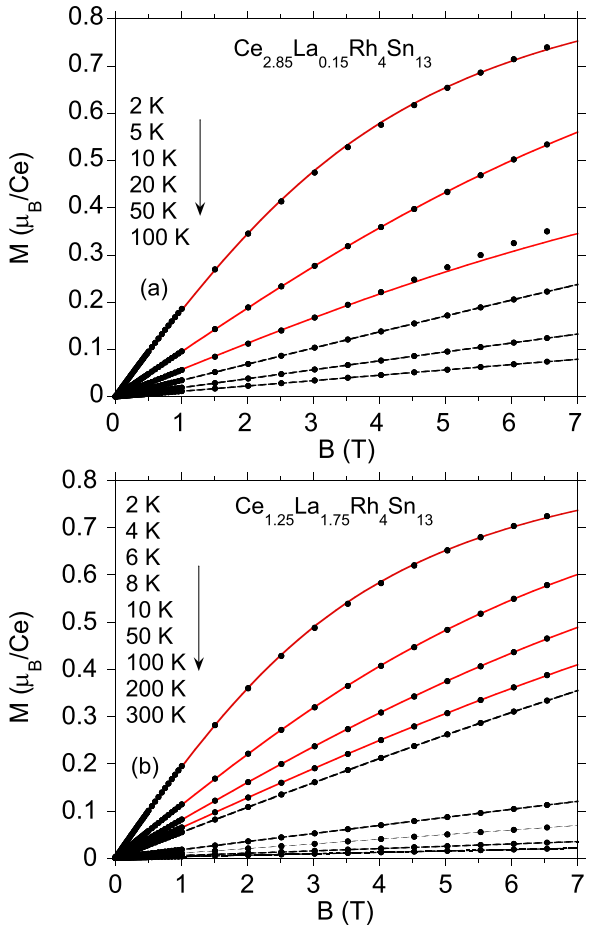

FIG. 9. (Color online) Magnetization M per formula unit vs magnetic field B measured at different temperatures for $Ce_{2.85}La_{0.15}Rh_4Sn_{13}$ and $Ce_{1.25}La_{1.75}Rh_4Sn_{13}$. The red solid lines are fits of the Langevin function to the magnetization data at the lowest temperatures.

the weak magnetic correlations of Ce magnetic moments in the cerium reach $Ce_{3-x}La_xRh_4Sn_{13}$ samples. Our interpretation of the magnetic data is based on the results from spin-polarized band-structure calculations, which showed a weakly magnetic ground state of $Ce_3Rh_4Sn_{13}$. Also, the calculated from the charge density analysis covalent bondings between Rh-Sn2 and Sn1-Sn2 atoms suggest deformation of the Sn_{12} cage, which will be used for interpretation of the magnetic susceptibility $\chi(T)$ data.

Figure 9 shows the magnetization M vs B isotherms for $Ce_{2.85}La_{0.15}Rh_4Sn_{13}$ and $Ce_{1.25}La_{1.75}Rh_4Sn_{13}$ characteristic of the paramagnets. They are well approximated by the Langevin function $L(\xi) = \coth(\xi) - 1/\xi$, where $\xi = \mu B/k_BT$ with total magnetic moment $\mu \approx 1\ \mu_B$ at $T = 1.8$ K and do not show any hysteresis in the field dependence of M. We note that the magnetization M is well approximated by the Langevin function for the all components of the $Ce_{3-x}La_xRh_4Sn_{13}$ series with $x \neq 0$. Figure 10 shows the temperature dependence of the dc magnetic susceptibility χ and inverse susceptibility data, $1/\chi$, for chosen samples of the $Ce_{3-x}La_xRh_4Sn_{13}$ series, measured in a magnetic field of 1000 Gs. The curvature in $1/\chi$ as well as a high-temperature effective moment slightly

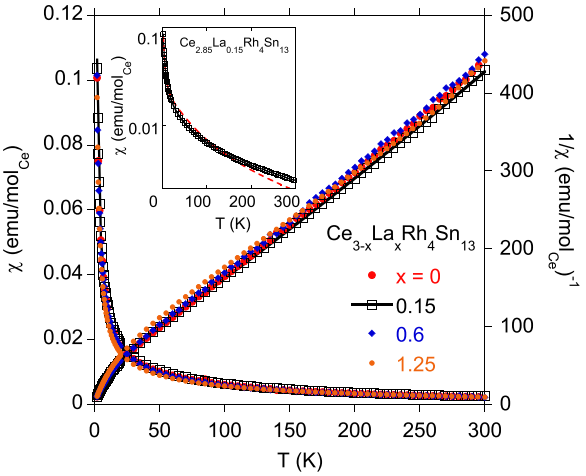

FIG. 10. (Color online) Magnetic susceptibility χ and $1/\chi$ of $Ce_{3-x}La_xRh_4Sn_{13}$ in external field of 1000 Gs. The red line represents the CEF fit to $1/\chi$ data for $Ce_{2.85}La_{0.15}Rh_4Sn_{13}$, with the two excited doublets separated from the ground-state doublet by energy $\Delta_1 = 40.5$ K and $\Delta_2 = 280.5$ K, respectively. In the inset, the dotted line shows the CEF fit to $\chi(T)$ data for the ground-state doublet (Γ_7) and excited quartet (Γ_8) separated by 107 K.

smaller than the value 2.54 μ_B expected for Ce^{3+} ion suggests the presence of both the crystalline-electric field (CEF) and Kondo effects. In a cubic environment, CEF will split the sixfold-degenerate Ce Hund's rule $J = 5/2$ into a Γ_7 doublet and a Γ_8 quartet [18]. An entropy analysis of the specific heat data (which will be discussed later) suggests the Γ_7 doublet as a ground state and a low-lying excited state. The fitted CEF susceptibility is given by the expression

$$\chi_{\rm CEF} = \frac{N(g_J\mu_B)^2}{Z}\left(\sum_{m\neq n}|\langle m|J_i|n\rangle|^2\frac{1-e^{-\beta\Delta_{mn}}}{\Delta_{mn}}e^{-\beta E_n} + \sum_n|\langle n|J_i|n\rangle|^2\beta e^{-\beta E_n}\right) + \chi_0, \quad (1)$$

where g_J is the Lande g factor, E_n and $|n\rangle$ are the nth eigenvalue and eigenfunction, respectively, J_i is a component of the angular momentum, and $\Delta_{mn} = E_n - E_m$, $Z = \sum_n e^{-\beta E_n}$ and $\beta = 1/k_BT$. In Fig. 10, this scenario (i.e., $\Gamma_7 - \Gamma_8$ CEF splitting) does not fit well the $\chi(T)$ data (the best fit represents the dotted line in the inset to the figure). The experimental $\chi(T)$ and $1/\chi(T)$ curves can be, however, well described in terms of CEF model considering the tetragonal Ce point symmetry, where the $J = 5/2$ multiplet of Ce^{3+} ion splits into three doublets separated from the ground state by energies $\Delta_1 \approx 40$ K and $\Delta_2 \approx 300$ K, respectively, and $\chi_0 \approx -0.00025$ emu/mol. The Van Vleck formula supplemented by the temperature-independent Pauli contribution χ_0 takes the form

$$\chi_{\rm CEF} = \frac{N\mu_B^2}{k_B}\frac{\sum_i\left(\frac{a_i}{T}+b_i\right)e^{-\beta\Delta_i}}{\sum_i g_i e^{-\beta\Delta_i}} + \chi_0, \quad (2)$$

where summations run over all i states of energies E_i and $\Delta_i = E_i - E_0$, and k_B is a Boltzman constant. Each thermally populated level contributes to the susceptibility: (i) by the low-frequency term, otherwise orientation, diagonal,

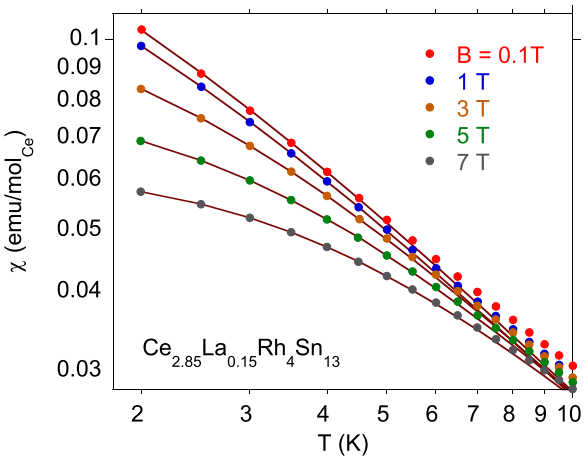

FIG. 11. (Color online) Magnetic susceptibility χ of $Ce_{2.85}La_{0.15}Rh_4Sn_{13}$ vs external magnetic field. The lines represent the fit of the resonance level Kondo model.

or Curie term a_i/T, or (ii) by the high-frequency term, otherwise polarization, off-diagonal, or Van Vleck term b_i. The first is the manifestation of the presence of a permanent magnetic moment (existing without the applied magnetic field), the second contribution is of polarization origin, and the corresponding magnetization is a sum of small induced moments that are collinear with the external field [19]. Fitting this expression to the experimental $1/\chi$ data (c.f. Fig. 10) yields the energy $\Delta_1 = 40.5$ K and $\Delta_2 = 280.5$ K for the sample $Ce_{2.85}La_{0.15}Rh_4Sn_{13}$, and similar CEF splitting for the other x components of the series. These Δ_1 and Δ_2 values are in reasonable agreement with that obtained from a neutron scattering study [20] and findings of Gamża *et al.* [12].

The low-temperature magnetic susceptibility as a function of T for various magnetic fields is plotted in Fig. 11. The $\chi(T)$ data are well approximated by *resonance level* Kondo model [21]. This model has a resonance of Lorenz shape and width Δ at the Fermi energy, which is roughly equal to the Kondo energy k_BT_K. Within the Kondo resonant-level model the susceptibility is expressed by

$$\chi = \frac{(g\mu_B)^2}{2\pi^2 k_B T}\mathrm{Re}\left\{(2S+1)^2\psi'\left[1+\frac{\Delta+ig\mu_BH}{2\pi k_BT}(2S+1)\right] - \psi'\left(1+\frac{\Delta+ig\mu_BH}{2\pi k_BT}\right)\right\}, \quad (3)$$

where ψ' is the first derivative of the digamma function. The fitting parameter Δ is field dependent and increases with increasing the field, which is typical for the single-ion Kondo system [22]. The level width Δ/k_B, e.g., for $Ce_{2.85}La_{0.15}Rh_4Sn_{13}$ is found to increase with magnetic field from 1.3 K to $\Delta/k_B = 4.2$ K for $B = 7$ T.

Figure 12 shows the specific heat of $Ce_{3-x}La_xRh_4Sn_{13}$ below 10 K as $C(T)/T$. The large value of $C(T)/T$ for $T \to 0$ typical for heavy Fermi liquid is characteristic for all $x \neq 0$ compounds of the series. The $4f$ contribution to the specific heat, $\Delta C(T)$, is well approximated by the Kondo resonant-level model [21]. Within this model the Kondo-impurity contribution ΔC with effective spin $S = 1/2$

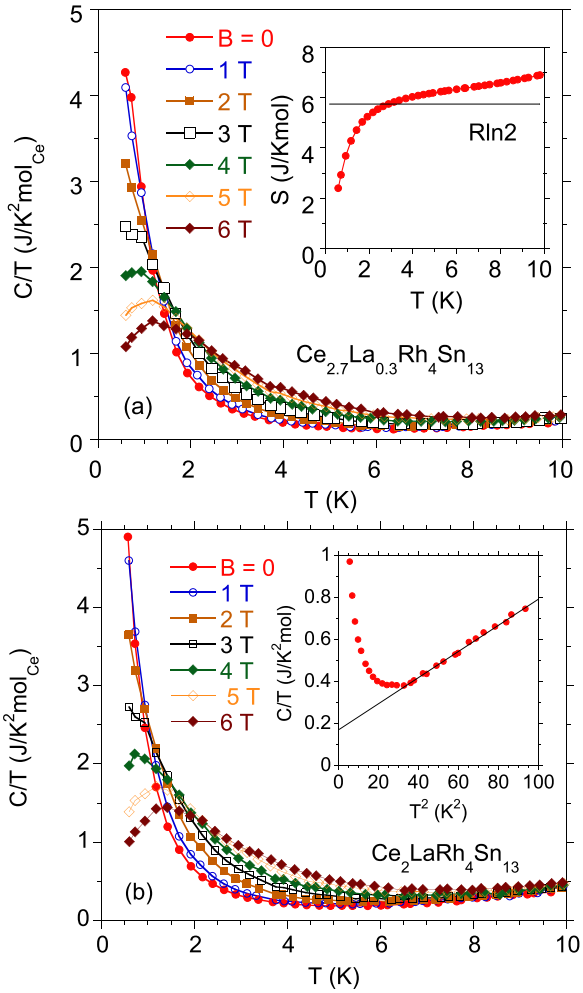

FIG. 12. (Color online) The low-temperature specific heat $C(T)/T$ for $Ce_{2.7}La_{0.3}Rh_4Sn_{13}$ (a) and $Ce_2LaRh_4Sn_{13}$ (b) in various applied magnetic fields. The inset in (a) shows the entropy vs temperature, in the lower panel the inset shows electronic specific heat $C(T)/T$ vs T^2.

is described by the formula

$$\Delta C = k_B\frac{2S\Delta}{\pi k_BT} - 2k_B\mathrm{Re}\left(\frac{(\Delta+ig\mu_BH)^2}{(2\pi k_BT)^2} \times\left\{(2S+1)^2\psi'\left[1+\frac{\Delta+ig\mu_BH}{2\pi k_BT}(2S+1)\right] - \psi'\left(1+\frac{\Delta+ig\mu_BH}{2\pi k_BT}\right)\right\}\right), \quad (4)$$

where R is the universal gas constant. The level width Δ/k_B is found to increase with magnetic field from about 0.5 K for $B = 0$ to about $\Delta/k_B = 2.3$ K for $B = 0.7$ T in the case of the investigated $Ce_{3-x}La_xRh_4Sn_{13}$ compounds (c.f. Fig. 13). Figure 14 shows the electronic coefficient in the specific heat, $\gamma_0^{\mathrm{exp}} \equiv C(T)/T$, obtained from the linear dependence of $C(T)/T = \gamma_0^{\mathrm{exp}} + \beta T^2$ (c.f. inset to Fig. 12) and the $\gamma_0^{\mathrm{calc}} = \frac{\pi^2}{3}k_B^2N(\epsilon_F)$, where $N(\epsilon_F)$ represents the density of electronic states at the Fermi level, calculated within the virtual crystal approximation. The distinct deviation between the γ_0

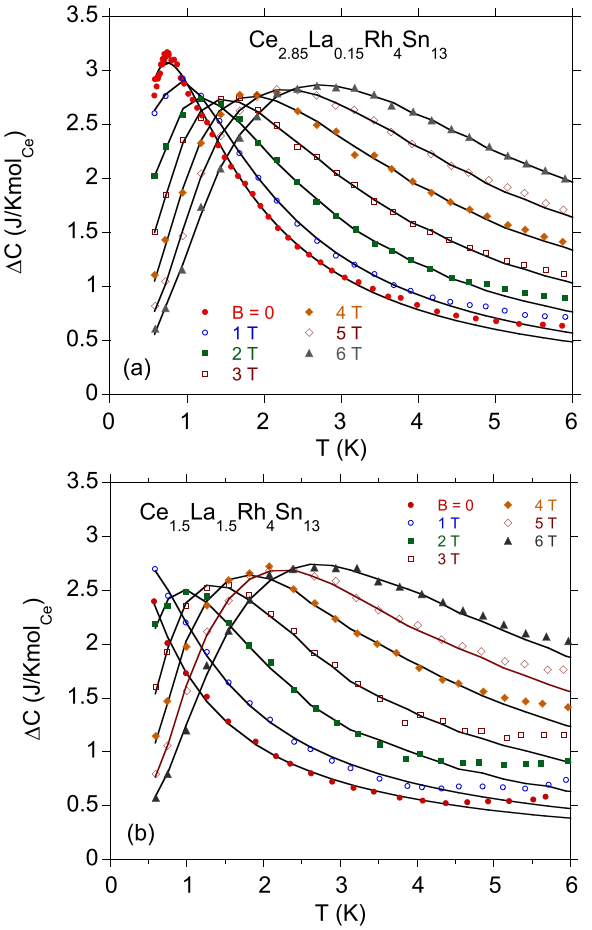

FIG. 13. (Color online) ΔC vs temperature in various applied magnetic fields. The lines represent the fit of resonance level model to experimental data.

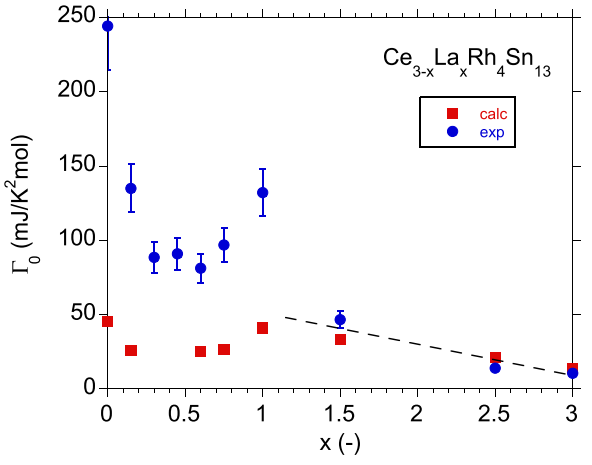

FIG. 14. (Color online) $Ce_{3-x}La_xRh_4Sn_{13}$ electronic specific heat coefficient $\gamma_0^{exp} \equiv C(T)/T$ experimentally obtained from the linear dependence of $C(T)/T$ vs T^2 at $T^2 = 0$ in the temperature region between ∼5 and ∼10 K (points) compared with the calculated Sommerfeld coefficient, using VCA approach within the FPLO method (squares).

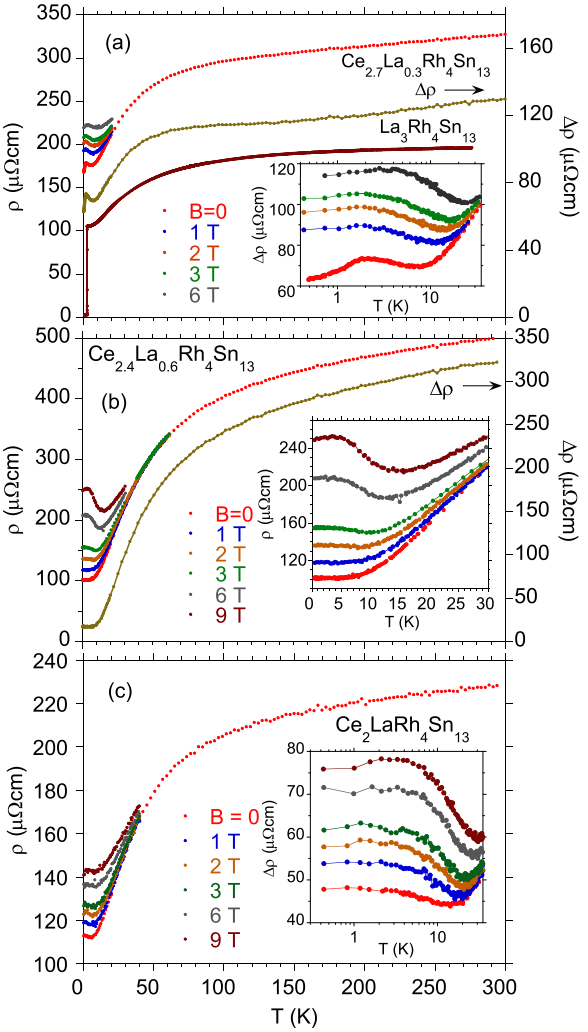

FIG. 15. (Color online) $Ce_{3-x}La_xRh_4Sn_{13}$ electrical resistivity $\rho(T)$ vs magnetic field for $Ce_{2.7}La_{0.3}Rh_4Sn_{13}$, $La_3Rh_4Sn_{13}$, and the difference $\Delta\rho = \rho(\text{sample}) - \rho(La_3Rh_4Sn_{13})$ at $B = 0$ (a), for $Ce_{2.4}La_{0.6}Rh_4Sn_{13}$ and the difference $\Delta\rho$ at $B = 0$ (b), and for $Ce_2LaRh_4Sn_{13}$ (c). The insets show the proper $\Delta\rho$ (or ρ) data vs log$T$ for $T < 30$ K.

values and VCA calculations indicates, for the samples $x \leqslant 1$, a strong f-electron correlation effect, which is not taken into account within the basic LSDA-based calculations. The γ's plotted across the Ce concentration range show a trend to the better agreement between the experimental and calculated γ values when the content of La increases, due to weakness of the f-electron correlations. From $\beta = \frac{12}{5}N\pi^4R\theta_D^{-3}$, we estimated a Debye temperature of about 180–200 K for the $Ce_{3-x}La_xRh_4Sn_{13}$ compounds.

Figure 15 displays the temperature dependence of the electrical resistivity ρ under applied magnetic fields for selected $Ce_{3-x}La_xRh_4Sn_{13}$ compounds. We also show the Ce $4f$ contribution to the resistivity $\Delta\rho = \rho(Ce_{3-x}La_xRh_4Sn_{13}) - \rho(La_3Rh_4Sn_{13})$ [23]. At higher temperatures, ρ of $La_3Rh_4Sn_{13}$ exhibits a significant deviation from the typical metallic behavior, which is often observed for the d-electron type metals [24] and could be attributed to the interband s-d scattering [25]. A similar interband s-d scattering is also

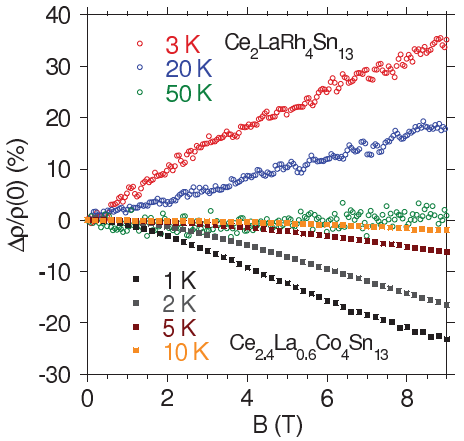

FIG. 16. (Color online) Magnetoresistivity $\Delta\rho/\rho(0)$ at different temperatures vs magnetic field for $Ce_2LaRh_4Sn_{13}$ (open circles) and $Ce_{2.4}La_{0.6}Co_4Sn_{13}$.

present in the remaining compounds of the $Ce_{3-x}La_xRh_4Sn_{13}$ system. Furthermore, the magnetic contribution $\Delta\rho$ can be associated both with the crystal field effect and coherence. The coherence is more significant for the samples with large Ce content (i.e., for $x \leqslant 0.3$) and will be discussed, while the CEF effect is apparent in all $\Delta\rho$ data, since the magnetic susceptibility measurements revealed a Schottky anomaly at similar temperatures.

The weak maximum in zero magnetic field resistivity at about 2 K suggests the magnetic scattering for the samples $x \leqslant 0.3$ [Fig. 15(a)], related to the incipient short-range magnetic ordering. For the sample $x > 0.3$, the magnetic correlations are weak or not present [c.f. Fig. 15(b)], whereas the more diluted Ce samples exhibit at the lowest temperatures the $\Delta\rho \sim -\ln T$ behavior, characteristic of the Kondo impurity effect [c.f. Fig. 15(c)]. The maximum that appears at ~4 K in the fields of 6 T can be attributed to the scattering on the Zeeman split of the crystal field ground doublet. We also observed below about 50 K the positive contribution to the magnetoresistance of $Ce_{3-x}La_xRh_4Sn_{13}$, which significantly increases with applied magnetic field. The mechanism of this positive magnetoresistance is not clear when the similar $Ce_3Co_4Sn_{13}$ [26] and $Ce_3Ru_4Sn_{13}$ [27] compounds exhibit the opposite behavior, and will be discussed below. In Fig. 16, we compare the magnetoresistivities $\Delta\rho/\rho(B=0)$, where $\Delta\rho = \rho(B) - \rho(B=0)$ of $Ce_2LaRh_4Sn_{13}$ [positive magnetoresistivity (MR)] and $Ce_{2.4}La_{0.6}Co_4Sn_{13}$ (negative effect) at different temperatures. One of the reasons may be the suppression of the coherence Kondo state by an external magnetic field, which causes an increase in resistivity at temperatures below the coherence maximum. It should be noted here that for a series of compounds $Ce_3M_4Sn_{13}$, where M = Co, Ru, and Rh, the coherence Kondo state is explicit in the resistivity data only for $Ce_3Rh_4Sn_{13}$ [28]. An increase of the resistivity of La-diluted $Ce_3Rh_4Sn_{13}$ with increasing magnetic field could also result from the so-called *magnetic precursor effect*, proposed to explain anomalous transport properties of some Gd-based intermetallics [29]. A magnetic disorder-induced localization of electrons can develop far before a magnetic order sets in. This is more probable scenario for La-doped $Ce_3Rh_4Sn_{13}$, which exhibit magnetic correlations of the magnetic moments of Ce. Such a localization implies a positive resistivity in applied fields. The positive ρ versus B increase is observed too for heavy fermions and Kondo lattices, as discussed in Ref. [29]

C. Physical discussion and summary

Our complex investigations of $Ce_{3-x}La_xRh_4Sn_{13}$ merely indicate on the changeover from a Kondo lattice state for $x \leqslant 0.3$ to a single-ion Kondo behavior state for $x > 0.3$. In the resistivity and specific-heat data, there is also observed a contribution from short-range magnetic correlations resulting from an atomic disorder. In this aspect, a La-diluted nonmagnetic heavy-fermion compound $CeNi_2Ge_2$ close to an antiferromagnetic QCP [30] would be interesting for the discussion of the low-temperature properties of $Ce_3Rh_4Sn_{13}$. Namely, this $Ce_{1-x}La_xNi_2Ge_2$ system exhibits two Fermi liquid (FL) regimes separated by a non-FL region for $0.5 \leqslant x \leqslant 0.98$, despite the absence of a magnetic order. The NFL-like behavior is, however, questionable since the low-lying magnetic phase transition has not been observed in this system. In the case of $Ce_3Rh_4Sn_{13}$, a number of experiments revealed, however, that the system evidently shows short-range magnetic correlations, therefore the low-temperature behaviors are of different origin in relation to $CeNi_2Ge_2$. In the literature are known examples of other Ce-based heavy fermions where La atoms diluting the $4f$-electron element were in fact found to produce a magnetic order of the spin-glass-like type, e.g., $Ce_{1-x}La_xCoGe_2$ [31] or $Ce_{1-x}La_xRhSb$ [32]. Similar short-range magnetic correlations observed recently [2,20] in $Ce_3Rh_4Sn_{13}$ are visible too for the isostructural substitution of Ce with La in $Ce_{3-x}La_xRh_4Sn_{13}$. Our complex studies also suggest that the system evolves from a magnetically correlated Kondo lattice state to a single-ion Kondo impurity state when the La content increases. This thinking allows us to analyze the $4f$ contribution to the specific heat, resistivity, and magnetic susceptibility in terms of the single-ion Kondo model. Note, however, that the inhomogeneous magnetic state of $Ce_3Rh_4Sn_{13}$ also suggests that the system could reach the magnetic ground state in the case of the weakly off-stoichiometric sample. Recently, our theoretical simulation of the vacancies at the Sn sites revealed that the magnetic ground state of $Ce_3Rh_4Sn_{13}$ is very sensitive to the Sn content [12]. Even slight nonhomogeneity or nonstoichiometry can result in different magnetic properties, as was investigated experimentally in Refs. [28,33,34]. The possible existence of a magnetic ordered phase has important consequences in the concept of quantum criticality in $Ce_3Rh_4Sn_{13}$ and similar materials. We have shown, however, that alloying does not give an antiferromagnetic quantum critical point in the $Ce_{3-x}La_xRh_4Sn_{13}$ system. In particular, the low-temperature specific-heat data, $C(T)/T$, do not demonstrate either power-law or $-\ln T$ behavior, moreover, the suite of experiments and theoretical analysis allow us to interpret the low-temperature behaviors in terms of the single-ion Kondo model. We also explained that the *magnetic character* of Ce ion is strongly dependent on its local environment. The difference charge density plots exhibit exceptionally strong charge accumulations located between the nearest-neighboring Sn2 and Rh, which implies covalent bonding interaction and leads to local deformation of the Sn_{12}

cages occupied by Ce (or Sn1). As a result of this local deformation of the cage, the thermodynamic properties of $Ce_{3-x}La_xRh_4Sn_{13}$ are determined by the CEF splitting of the $J = 5/2$ multiplet into three doublets separated by energies $\Delta_1/k_B \approx 40$ K and $\Delta_2/k_B \approx 300$ K from the ground-state doublet. The Kondo lattices are usually discussed in terms of the two temperature scales: the usual single-impurity Kondo scale and the coherence, both depend on the CEF. The first is responsible for $T_{\min}$ and $\rho \sim -\ln T$, while the coherence is reflected in $T_{\max}$ in the $\rho(T)$ curves. At low temperature, in a Kondo lattice system, there is a competition between a tendency for the resistivity to increase due to Kondo effect and to decrease because of the singlet nature of the coherent ground state. $T_{\max}$ obtained from the $\Delta\rho$ resistivity data represents a good characteristic of T_K (for the Kondo lattice, T_K at a higher temperature region represents a Kondo effect on the total $J = 5/2$ manifold, to distinguish the high-T T_K we use the notation T_K^J). In the case of $Ce_3Rh_4Sn_{13}$, $T_{\max} \sim 50$ K. In the Kondo lattice state, $T_K = \frac{W}{2}\exp[-\frac{1}{J_K N(\epsilon_F)}]$, where W is the bandwidth of the bare band (s,d) states with DOS at ϵ_F equal to $N(\epsilon_F)$. The value J_K is the Schrieffer-Wolf exchange coupling integral [35], for $V, \epsilon_f \ll U$, $J_K \sim -|V|^2/\epsilon_f$, where ϵ_f is the bare $4f$ level location with respect to the Fermi level and U is the magnitude of the intra-atomic $(f$-$f)$ Coulomb repulsion between electrons. A very crude estimate gives T_K^J of ~70 K, using the data obtained from the $3d$ XPS spectra and DOS calculations. Using $\Delta_{fs} \cong 70$ meV and ϵ_f of about 0.1 eV, we estimated $J_K = \sim 0.009$ eV. For $N(\epsilon_F) \approx 201/\text{eV}$ and the bandwidth of about 4 eV, we roughly have estimated T_K^J value, which corresponds to the Kondo effect on the total $(J = 5/2)$ manifold. Based on this very crude estimate, we can suggest a possible scenario to explain the resistivity increase below 70 K in an applied magnetic field.

Let us apply the above results to the following discussion of the experimental data. The system $Ce_{3-x}La_xRh_4Sn_{13}$ exhibits very similar $C(T)/T$ and $\chi(T)$ dependencies. (i) The curvature in $\chi(T)$ can be well described in terms of a CEF model considering the lower than cubic symmetry where the $J = 5/2$ multiplet of Ce^{3+} ion splits into three doublets separated from the ground state by energies $\Delta_1/k_B \approx 40$ K and $\Delta_2/k_B \approx 300$ K. The resistivity of $Ce_{3-x}La_xRh_4Sn_{13}$ samples with $x = 0$ and $x = 0.3$ clearly shows the maximum at about 50 K due to the Kondo coherence effect. The coherent state is affected by an external field, then because of the suppression of the coherent Kondo effect, the resistivity would increase. There is also a possible *magnetic precursor effect*, which leads to an enhancement of the magnetoresistivity under increasing magnetic field, or both effects. A clear-cut answer, however, requires modeling on the basis of theoretical research. The strong positive magnetoresistivity can also result from the d-band character of the conduction electrons, and the strong s-d hybridization. Such a scenario is well confirmed experimentally for isostructural $Y_3Ir_4Ge_{13}$, where the MR is positive [36] as in the case of $Ce_3Rh_4Sn_{13}$. Strydom (Ref. [36]) interprets the positive MR behavior as a result of strong d-electron interaction in a d-electron transition metal, which could be brought about by a large d band spectral weight of the conduction electrons. This interpretation requires a confirmation by the band-structure calculations (these studies are in progress), but it seems that this scenario can also be justified experimentally. Namely, our systematic studies of the $Ce_3M_4Sn_{13}$ intermetallics have shown that the MR effect depends on the metal M; in the case of Co, the MR is negative [26], for Ru, the magnetoresistivity is very small, but positive [27] (at the low-temperature region $\Delta\rho/\rho(0) \approx +1\%$), while for Rh, the MR exhibits a strong positive effect. (ii) The low-temperature magnetic susceptibility and specific heat are well fitted by a Kondo resonant-level model with a very small Kondo resonance width Δ/k_B of about 1 K. The zero-field resistivity suggests at the lowest temperatures the presence of short-range magnetic correlations, which are easily removed by the magnetic field. Our complex investigations do not confirm a long-range magnetic order and the presence of a quantum critical point in the system $Ce_{3-x}La_xRh_4Sn_{13}$.

The results (i) and (ii) are consistent with our band-structure calculations and the XPS data. The Ce $3d$ XPS spectra point to a stable configuration of the Ce $4f^1$ shell and a weak hybridization between the $4f$ and the conduction band states, which well correlates with the Kondo effect and coherence, both observed at relatively low temperatures. The chemical bondings between Rh and Sn2 resulting from the calculated charge density distribution explain the deformation of the $Ce(Sn2)_{12}$ cuboctahedra cages and the CEF properties of the $Ce_{3-x}La_xRh_4Sn_{13}$ compounds.

ACKNOWLEDGMENT

We thank National Science Centre (NCN) for financial support, on the basis of decision No. DEC-2012/07/B/ST3/03027.

[1] N. F. Mott, *Metal-Insulator Transitions* (Taylor and Francis, London, 1990).
[2] U. Köhler, A. P. Pikul, N. Oeschler, T. Westerkamp, A. M. Strydom, and F. Steglich, J. Phys.:Condens. Matter **19**, 386207 (2007).
[3] E. L. Thomas, H.-O. Lee, A. N. Bonkston, S. MaQuilon, P. Klavins, M. Moldovan, D. P. Young, Z. Fisk, and J. Y. Chan, J. Sol. State Chem. **179**, 1642 (2006).
[4] A. L. Cornelius, A. D. Christianson, J. L. Lawrence, V. Fritsch, E. D. Bauer, J. L. Sarrao, J. D. Thompson, and P. G. Pagliuso, Physica B **378–380**, 113 (2006).
[5] P. W. Anderson, Phys. Rev. **124**, 41 (1961).
[6] J. KondoProg. Theoret. Phys. **32**, 37 (1964).
[7] J. P. Remeika, G. P. Espinosa, A. S. Cooper, H. Barz, J. M. Rowel, D. B. McWhan, J. M. Vandenberg, D. E. Moncton, Z. Fizk, L. D. Woolf, H. C. Hamaker, M. B. Maple, G. Shirane, and W. Thomlinson, Sol. State Commun. **34**, 923 (1980); J. L. Hodeau, M. Marezio, J. P. Remeika, and C. H. Chen, *ibid.* **42**, 97 (1982).
[8] J. Rodriguez-Carvajal, Physica B **192**, 55 (1993).
[9] A. Ślebarski and J. Goraus, Phys. Rev. B **88**, 155122 (2013).

[10] K. Koepernik and H. Eschrig, Phys. Rev. B **59**, 1743 (1999); I. Opahle, K. Koepernik, and H. Eschrig, *ibid.* **60**, 14035 (1999); K. Koepernik, B. Velicky, R. Hayn, and H. Eschrig, *ibid.* **55**, 5717 (1997); H. Eschrig, K. Koepernik, and I. Chaplygin, J. Solid State Chem. **176**, 482 (2003); www.fplo.de.
[11] J. P. Perdew and Y. Wang, Phys. Rev. B **45**, 13244 (1992).
[12] M. Gamża, W. Schnelle, A. Ślebarski, U. Burkhardt, R. Gumeniuk, and H. Rosner, J. Phys.:Condens. Matter **20**, 395208 (2008).
[13] O. Gunnarsson and K. Schönhammer, Phys. Rev. B **28**, 4315 (1983).
[14] J. C. Fuggle, F. U. Hillebrecht, Z. Zolnierek, R. Lässer, Ch. Freiburg, O. Gunnarsson, and K. Schönhammer, Phys. Rev. B **27**, 7330 (1983).
[15] A. Ślebarski, T. Zawada, J. Spałek, and A. Jezierski, Phys. Rev. B **70**, 235112 (2004).
[16] C. S. Lue, H. F. Liu, S.-L. Hsu, M. W. Chu, H. Y. Liao, and Y. K. Kuo, Phys. Rev. B **85**, 205120 (2012).
[17] L. E. Klintberg, S. K. Goh, P. L. Alireza, P. J. Saines, D. A. Tompsett, P. W. Logg, J. Yang, B. Chen, K. Yoshimura, and F. M. Grosche, Phys. Rev. Lett. **109**, 237008 (2012).
[18] K. R. Lea, M. J. K. Leask, and W. P. Wolf, J. Phys. Chem. Solids, **23**, 1381 (1962).
[19] J. Mulak, J. Less-Common Met. **121**, 141 (1986).
[20] D. T. Adroja, A. M. Strydom, A. P. Murani, W. A. Kockelmann, and A. Fraile, Physica B **403**, 898 (2008).
[21] K. D. Schotte and U. Schotte, Phys. Lett. **55**, 38 (1975).
[22] P. D. Sacramento and P. Schlottmann, Phys. Rev. B **40**, 431 (1989).
[23] Note that the measured resistivities of both $Ce_3Rh_4Sn_{13}$ and $La_3Rh_4Sn_{13}$ contain defect related resistivities due to disorder and structural defects (off stoichiometry, c.f., Ref. [12]), this contribution is not taken into account, even though it is not negligible. We considered similar defects for the system of $Ce_{1-x}La_xRh_4Sn_{13}$ alloys.
[24] F. Canepa and S. Cirafici, J. Alloys Compd. **232**, 71 (1996).
[25] N. F. Mott, Proc. R. Soc. A **153**, 699 (1936).
[26] A. Ślebarski, M. Fijałkowski, and J. Goraus, Intermetallics **54**, 199 (2014).
[27] A. Ślebarski, M. Fijałkowski, J. Goraus, L. Kalinowski, and P. Witas, J. Alloys Compds. **615**, 921 (2014).
[28] A. Ślebarski, B. D. White, M. Fijałkowski, J. Goraus, J. J. Hamlin, and M. B. Maple, Phys. Rev. B **86**, 205113 (2012).
[29] R. Mallik and E.V. Sampathkumaran, Phys. Rev. B **58**, 9178 (1998).
[30] A. P. Pikul, U. Stockert, A. Steppke, T. Cichorek, S. Hartmann, N. Caroca-Canales, N. Oeschler, M. Brando, Ch. Geibel, and F. Steglich, Phys. Rev. Lett. **108**, 066405 (2012).
[31] C. R. Rotundu and B. Andraka, Phys. Rev. B **74**, 224423 (2006).
[32] A. Ślebarski, J. Spałek, M. Fijałkowski, J. Goraus, T. Cichorek, and Ł. Bochenek, Phys. Rev. B **82**, 235106 (2010).
[33] Y. Ōduchi, C. Tonohiro, A. Thamizhavel, H. Nakashima, S. Morimoto, T. D. Matsuda, Y. Haga, K. Sugiyama, T. Takeuchi, R. Settai, M. Hagiwara, and Y. Ōnuki, J. Magn. Magn. Mater. **310**, 249 (2007).
[34] J. Custers, M. Kriegisch, M. Müller, A. Thamizhavel, A. M. Strydom, and S. Paschen, Physica B, **403**, 1312 (2008).
[35] J. R. Schrieffer and P. A. Wolff, Phys. Rev. **149**, 491 (1966).
[36] A. M. Strydom, J. Phys.: Condens. Matter **19**, 386205 (2007).